Research Square

Preprints are preliminary reports that have not undergone peer review.
They should not be considered conclusive, used to inform clinical practice,
or referenced by the media as validated information.

Early α-synuclein pathology induces disease-associated microglia and non-cell-autonomous alteration of midbrain dopamine neurons

Linda Gillberg
Karolinska Institutet
Behzad Yaghmaeian-Salmani
Karolinska Institutet
Isabel Hemming
Karolinska Institutet
Laura Lahti
Karolinska Institutet
Niclas Branzell
Karolinska Institutet
Silke Nuber
Brigham and Women's Hospital
Dennis Selkoe
Brigham and Women's Hospital
Per Svenningsson
Karolinska Institutet
Thomas Perlmann
thomas.perlmann@ki.se
Karolinska Institutet

Research Article

Keywords: Alpha-synuclein, Parkinson's disease, Disease-associated microglia, Neuroinflammation, Midbrain dopamine neurons, Galectin-3, Single-cell/-nucleus RNA sequencing, PLX3397, 3K-hα-syn

Posted Date: November 19th, 2026

DOI: https://doi.org/10.21203/rs.3.rs-11539990/v1

License: This work is licensed under a Creative Commons Attribution 4.0 International License.
Read Full License

Additional Declarations: No competing interests reported.

Abstract

Parkinson's disease (PD) is characterised by alpha-synuclein (α-syn) aggregation, degeneration of midbrain dopamine (mDA) neurons, and neuroinflammation. Here, we investigated the ventral midbrain of mice heterozygous for an aggregation-prone mutated form of human α-syn(3K-hα-syn) expressed via the Thy1 promoter. Immunohistochemical analysis revealed that 3K-hα-syn accumulated predominantly in non-dopaminergic neurons of the ventral midbrain, most notably within the red nucleus, while neighbouring mDA neurons showed no detectable transgene expression or phosphorylated α-syn. Despite this, robust microgliosis was observed broadly in the ventral midbrain. Single-nucleus RNA sequencing of mDA neurons demonstrated preserved mDA neuron subtype architecture but selective induction of cholesterol biosynthesis pathways together with downregulation of synaptic gene programmes. In parallel, single-cell RNA sequencing of CD45 + immune cells from the ventral midbrain revealed a transition towards a disease-associated microglial (DAM) state characterised by upregulation of *Apoe, Lgals3, Fabp5*, and inflammation-associated pathways. Histological analysis showed that Galectin-3-positive DAM accumulated over time in regions with pronounced levels of phosphorylated α-syn. Finally, pharmacological depletion of microglia using the colony-stimulating factor 1 receptor (CSF1R) inhibitor PLX3397 selectively worsened beam-traversal performance in female *3K^{het}* mice, supporting a sex-dependent protective contribution of microglia. Together, these findings demonstrate pathological α-syn accumulation coinciding with widespread microglial activation and suggest that microglia can exert context- and sex-dependent beneficial effects during early stages of 3K-hα-syn-driven neuropathology.

Introduction

Parkinson's disease (PD) is the most prevalent movement disorder and the second most common neurodegenerative disease, affecting 2–3% of the population over 65, and with rising incidence in an ageing population [1]. The selective degeneration of midbrain dopamine (mDA) neurons in the substantia nigra pars compacta (SNpc) along with progressive striatal dopamine depletion, results in the defining motor symptoms of PD: bradykinesia, rigidity, and resting tremor. These symptoms are often alleviated by dopaminergic medications [2]. At the cellular and molecular level, PD is characterised by the intracellular accumulation of misfolded alpha-synuclein (α-syn) in insoluble aggregates called Lewy bodies and Lewy neurites, which also contain abundant lipid membrane fragments and represent the neuropathological hallmark of the disease[3]. The pathology affects the SNpc but progressively involves several other brain regions [4–6].

The causal role of α-syn in PD was established by the discovery of missense point mutations in *SNPCA* in familial forms of the disease [7]. The initial finding was followed by the identification of other missense mutations and genetic *SNPCA* multiplication events. Collectively, these genetic findings have motivated the development of mouse models expressing mutant α-syn as platforms for studying disease mechanisms. Among these, the 3K-hα-syn mouse model was generated by introducing three glutamate-

to-lysine substitutions (E35K, E46K, E61K) into the conserved N-terminal KTKEGV-like repeat motifs of human *SNPCA* cDNA sequence in a mouse transgene driven by the Thy1 neuronal promoter [8]. These mutations collectively shift the conformational equilibrium towards a protein predisposed to pathological phosphorylation and aggregation [8,9]. Heterozygous (*3K^{het}*) mice develop progressive accumulation of serine-129 phosphorylated α-syn (pα-syn; also found in human Lewy bodies) and exhibit behavioural abnormalities that are partially alleviated by L-Dopa. Thus, *3K^{het}* mouse is an experimentally tractable model for investigating the molecular and cellular consequences of α-syn accumulation and toxicity *in vivo*.

Neuroinflammation has emerged as a cardinal and early feature of PD pathology that actively contributes to the disease process [10]. Activated microglia in the SNpc were first documented in postmortem PD brain tissue more than three decades ago [11] and have since been confirmed in living patients through positron emission tomography imaging using radioligands that bind to and mark microglial activation [12]. Genome-wide association studies have further implicated microglial biology in PD risk, with gene variants converging on innate immune pathways including *LRRK2*, and *HLA-DRA* [13]. Nevertheless, the microglial response in PD is not a uniform cellular state; rather, microglia adopt a spectrum of transcriptional and functional identities depending on disease stage, brain region, and the nature of the pathological signal they encounter [10].

One particularly well-characterised reactive state that has attracted substantial interest is the disease-associated microglial (DAM) phenotype, first described through single-cell transcriptomics in mouse models of Alzheimer's disease [14,15]. DAM is defined by a conserved transcriptional programme that includes upregulation of markers including *Apoe*, *Lgals3*, *Trem2*, *Clec7a*, *Lpl*, *Cst7*, *Fabp5*, and *Itgax* [16,17]. DAM have subsequently been identified across neurodegenerative conditions beyond Alzheimer's disease, including PD, amyotrophic lateral sclerosis, frontotemporal dementia, multiple sclerosis, and prion disease [16]. In the context of synucleinopathy, Galectin-3, encoded by the *Lgals3* gene, is one of the most upregulated DAM marker genes and has been detected in activated microglia associated with α-syn pathology in human PD postmortem brain and in experimental models. Galectin-3 has been implicated in regulating inflammatory signalling, phagocytosis and neurodegeneration [18]. However, although DAM microglial states have been described in several mouse α-syn models, how DAMs develop spatially and temporally in relation to the distribution of pathological α-syn remains incompletely understood.

A central and unresolved question is whether the microglial activation observed in PD and related models is always promoting neurodegeneration or if it can be neuroprotective. In rodent models of α-syn toxicity, several studies have used pharmacological depletion of microglia using inhibitors of CSF1R. Overall, these reports support that microglial-mediated neuroinflammation can promote disease progression; however, some show neutral or more complex outcomes [19–22]. An additional dimension of complexity is introduced by biological sex: PD affects men at approximately 1.5-fold higher rates than women, and disease progression and symptom profiles differ between men and women. The reasons

behind these differences are unknown, but microglia may contribute as they are themselves sexually dimorphic in their gene expression, morphology, and functional responses [23,24]. However, whether sex modulates the nature or functional consequences of the DAM response in synucleinopathies has not been thoroughly investigated.

In the present study, we characterise the spatial and temporal dynamics of 3K-hα-syn pathology and the accompanying microglial response in *3K^{het}* mice. Ventral midbrain mDA neurons and microglial cells were analysed using single-nucleus and single-cell transcriptomics, respectively, along with histological examination to reveal the progressive accumulation of the neuroinflammatory response. We also pharmacologically depleted the microglia with the CSF1R inhibitor PLX3397 to study its effect on motor performance. These findings provide a framework for understanding early microglial responses in a synucleinopathy and identify sex as a critical biological variable in the functional outcome of neuroinflammation.

Materials and Methods

Mouse strains and genotyping

3K [8], *Slc6a3^{Cre}* [48], and *Rpl10a-mCherry* (*TrapC^{flox}*) [49] mouse lines and their genotyping have been described. The mice were maintained on C57BL/6J (RRID:IMSR_JAX:000664) background and crossed and intercrossed to create *Slc6a3$^{Cre/+}$*; *TrapC$^{flox/flox}$* (control), and *Slc6a3$^{Cre/+}$*; *3K^{het}*; *TrapC$^{flox/flox}$* (*3K^{het}*) strains. Control mice were littermates with no 3K allele. Both female and male mice were analysed in all experiments.

Immunohistochemistry

The mice were deeply anaesthetised and perfused intracardially with 37C DPBS (Gibco 14190144) followed by 37C 4% paraformaldehyde (PFA, Sigma-Aldrich P6148) in DPBS. The brain was cut coronally in three parts using a brain matrix (AgnTho's 69-2165-1) and post-fixed over two nights at RT, with PFA changed the following day after perfusion. The brains were dehydrated and processed into Histosec wax without DMSO (Merck, 101676) using an automated tissue processor (Leica TP1020). Sections were cut at 6 µm using an automated rotating waterfall microtome (Epredia HM355S) and collected on Superfrost Plus slides (Menzel-Gläser, 631–9483). Gal3 (R&D Systems AF1197, 1:600), Iba1 (Invitrogen PA5-27436 or Abcam ab318302, both 1:600), and TH (Millipore MAB318 1:600) co-stainings were performed as described [50]. For the detection of human alpha-synuclein (ENZO ALX-804-258-L, 1:30), phospho-alpha-synuclein S129 (Abcam AB51253, 1:300 dilution), and TH (Pel-Freez P60101-0, 1:400) the PBS was substituted with TBS (Medicago 09-7500-100) and the heat-mediated antigen retrieval was substituted with permeabilization in 0.3% Triton X-100 (Sigma-Aldrich 93443) in TBS. Secondary antibodies (all 1:400) were either from Jackson Immunoresearch: donkey anti-rabbit Cy3 (711-165-152), donkey anti-mouse Alexa Fluor 488 (715-545-150), donkey anti-rat Cy3 (712-165-163), donkey anti-goat Alexa Fluor

647 (705-604-147), or from Invitrogen: donkey anti-chicken Alexa Fluor 647 (A21449) and donkey anti-sheep Alexa Fluor 647 (A21448). DAPI (Roche 59795022, 1 mg/ml in double distilled water) was added together with the secondary antibodies at 1:1000. The images were taken on a Zeiss LSM700 confocal microscope or Zeiss AxioImager widefield fluorescent microscope. The analyses were performed on original raw files. For the figure panels, the brightness and contrast were adjusted, if necessary, either in Photoshop (Adobe, v26.1.0) or in Fiji (ImageJ2 v2.9.0/154d). The tiling of images was done either using the automated photomerge -function in Photoshop or by pairwise stitching[51] in Fiji.

Quantification of Iba1 + and Gal3 + microglia

Images sized 1280x1280 µm were scanned in the approximate region of red nucleus throughout the midbrain, keeping the confocal settings same for all the samples. The ratio of Iba1 and Gal3 signal to the entire image area was calculated in Fiji after automated thresholding. Five images from each brain were analysed and their values averaged for the statistical analysis. The homoscedasticity was analysed using Levene's test, and normal distribution using Shapiro-Wilk test. One-way ANOVA with Tukey simultaneous test for differences of means was carried out with default parameters. The details of statistical tests and *P*-values are found in Supplementary Table 12.

Isolation of dopaminergic neurons and immune cells

Slc6a3 $^{Cre/+}$; *3K*^{het}; *TrapC*$^{flox/flox}$ (n = 2) and littermate control (n = 2) mice were euthanized with CO_2, and brains were quickly collected into ice-cold oxygenated cutting solution [52]. The tissue was sectioned in 375 µm thick coronal slices on a vibratome (VT1000S, Leica) and the midbrain area of interest dissected out from each slice. One hemisphere of midbrain was collected into DNA LoBind tubes (Eppendorf), quickly chilled on dry ice and stored at -80 °C for nuclei preparation; the other was dissociated into single cell suspension using Neural tissue dissociation kit (P) (Miltenyi Biotec), followed by staining with APC-CD45 antibody (BioLegend 103111, 1:150) for 15 min at 4 °C, washed and resuspended into HBSS containing 2% FBS and 0.8% glucose. The cell suspension was filtered on a 35 µm filter and stained with DAPI (Merck, 1:500) before being analysed and sorted on FACS. Nuclei preparation was performed as described previously [27] and stained with DAPI 5 min before being sorted. The flow cytometry sorting and analysis was performed at the Biomedicum Flow cytometry Core facility that receives funding from the Infrastructure Board at Karolinska Institutet. A FACSAria Fusion cell sorter with the FACSDiva software (BD Biosciences) was used for both cell and nuclei sorting. Cells were identified by forward- and side-scatter gating, a 405 nm laser with a 450/50 filter, and a 640 nm laser with a 670/30 filter, quantifying DNA content per event to assure that only singlets were collected. For nuclei, a 561 nm laser with a 610/20 filter was also used. A 100 µm nozzle and an acquisition rate of ~ 4000 (cells) or 1000 (nuclei) events per second was used for sorting. Sorted cells/nuclei were preserved in 2% BSA until downstream procedures.

Library preparations and sequencing

Chromium single cell 3´v3, dual indexing (10X Genomics) was used to make libraries in accordance with the manufacturer´s protocol. Libraries were sequenced on a NovaSeqXPlus system (NGI, SciLifeLab, Karolinska Institute). Library preparation and sequencing for nuclei and cells were done separately.

Quantification of Cd45 + cells using FACS

Additional samples (n = 3 each for *Slc6a3*$^{Cre/+}$; *3K*^{het}; *TrapC*$^{flox/flox}$ and control littermates) were prepared as stated for isolation of immune cells and analysed on FACSAria Fusion without collecting cells. All FACS fcs-files were analysed by FlowJo (BD Biosciences, v10.10.0) to quantify amount of cd45 + cells in each sample, using the plugin DownSampleV3 on the single cell gate to have comparable number of cells from all samples. Differences between group was analysed with unpaired t-test.

Bioinformatic analyses and statistics

Sequenced reads were demultiplexed and aligned to a customized reference package based on GRCm39_2024A, using cellranger-6.1.2 (10x Genomics). Seurat package version 4 was used for downstream analyses of the data [53].

Microglia QC and analysis

Each scRNA sample was filtered based on these parameters to remove low-quality libraries [nFeature_RNA > 90, nCount_RNA > 120, UMIsperGene > 1.3, percent_mito < 20]. To minimize sparsity, genes with zero total counts across all cells were also removed from downstream analysis. Next, predicted doublets were removed and samples were merged into one dataset. The data was split by sex (1 male, 1 female sample per genotype), and each subset was independently normalized with variable features (n = 3000) identified via SCTransform [54] while regressing out mitochondrial percentage. Next, datasets were integrated using Seurat v4 anchor-based integration (FindIntegrationAnchors and IntegrateData), using "CCA" (Canonical Correlation Analysis) method. Next, PCA was calculated for the integrated assay, and elbowplot was used to detect the range of principal components that retain most of the meaningful biological variance (PCs 1:19). The same PCs range was used to construct a shared nearest neighbour (SNN) graph and to identify clusters by Louvain; “SNN” modularity optimization-based clustering algorithm. Non-linear dimensionality reductions (UMAP, tSNE) were done using the same range of PCs and other default parameters. The optimal clustering resolution (0.3) was determined using normalized Silhouette (“cluster” package version 2.1.6 Maechler et al., 2023.) and Calinski-Harabasz (“fpc” package version 2.2–14; Hennig C. 2026) scores. After initial data visualization, clusters 3 and 6 were further sub-clustered using Louvain algorithm at resolution 0.1, each divided into two subclustered, yielding a total of 10 clusters. The final 10 clusters were ordered by size and renamed from 0 to 9 and added to metadata as “seurat_clusters”.

Midbrain Neurons QC and analysis

Each snRNA sample was filtered based on these parameters to remove low-quality libraries [nFeature_RNA > 600, nCount_RNA > 1000, nCount_RNA < 3.5e4, percent_mito < 5]. Genes with zero total counts across all cells were also removed from downstream analysis to minimize sparsity. Next, predicted doublets were removed and samples were merged into one dataset, which was later log normalized. 3000 highly variable genes were identified using VST method. The data was subset based on the HVGs for conversion to AnnData which was later used as input for scvi-tools (single-cell variational inference tools, version 1.2.0) which is a modelling tool based on stochastic optimization and deep neural networks [50,51]. The model was set up with batch_key="sex", n_layers = 2, n_latents = 50, dropout_rate = 0.05, and gene_likelihood = Negative binomial. The model was trained with max_epochs of 100, and early stopping. Next, the latent representations were extracted from the model and inserted into the original Seurat object as a new reduced dimension with the name: key = "scvi_". Singular Value Decomposition (SVD) was performed on the model's latent representations and singular values were used to calculate the explained variance as [singular_values^2 / sum(singular_values^2)]. Then cumulative variance was calculated and plotted against the number of singular values to pick the point where the curve plateaus and more than 98% of variance is captured. Based on this approach scvi_dims 1:28 were selected for downstream analyses, including Shared Nearest-neighbor (SNN) graph construction, and unsupervised Louvain clustering. The optimal clustering resolution (0.4) was determined using normalized Silhouette and Calinski-Harabasz scores. Dims 1:25 were used for non-linear dimensionality reductions (UMAP, tSNE) because including dims 26:28 made the 2D visualization slightly noisier.

Annotation of Midbrain Neurons

We used a well-annotated dataset (intact) from our previous study[27] to do reference mapping on the midbrain neurons by transferring cell type labels (mDA neighbourhoods) and projecting the midbrain neurons dataset (query) onto the pre-existing, well-annotated intact dataset, using Seurat package V4. More than 94% of the cells in the query had a prediction.score.max ≥ 0.5, showing a reasonably confident label transfer. Pooled territory labels were made based on the neighbourhood label assignment from the same territory [27].

Doublet predictions

DoubletFinder v-2.0.6 was used to predict potential doublets per sample after initial filtering. In the parameter selection phase, artificial doublets were generated and incorporated, PCA was calculated, optimal PC range determined by elbowplot and used in paramSweep() step to calculate the proportions of artificial k nearest neighbours (pANN). To identify optimal pK values without ground-truth doublet information (GT = FALSE), the mean-variance normalized bimodality coefficient (BC_{MVN}) was calculated and optimal pK was selected by BC_{MVN} maximization [55]. In the doublet classification phase, the total number of heterotypic doublets are estimated from the Poisson doublet formation rate with homotypic

doublet adjustment. Homotypic doublets are estimated by the optimal resolution from unsupervised Louvain clustering outcomes which is selected based on either normalized Silhouette or Calinski-Harabasz scores.

Pseudobulk DE analysis

To better account for both sample-level and cell-level overdispersions in DE analysis between *3k*^{het} and *control*, we used Negative Binomial mixed model Using a Large-sample Approximation (NEBULA, v-1.5.6) [56]. Seurat data was converted to a Nebula dataset via an “SCE” dataset, using SingleCellExperiment v-1.28.1. Sample IDs were set as the random effect, nCount_RNA was set as offset to account for library size differences, while fixed effect predictors were genotype and sex. Nebula was run with these parameters [model = "NBGMM",

method = "HL", cutoff_cell = 20, kappa = 800, covariance = TRUE, output_re = TRUE]. From Nebula’s result, model coefficients were extracted, the covariance matrix was reconstructed, and a Wald contrast function was written for a genome-wide Wald test for the genotype effect averaged across sexes, obtained from Nebula’s negative binomial generalized linear mixed model. The contrast estimates the difference between *3K*^{het}, and *ctrl* averaged over male and female cells (β_genotype3k + (0.5 x β_genotype3k:sexmale)). Another contrast was written for sex effect averaged across genotypes, estimating the difference between male and female cells averaged over *3K*^{het}, and *ctrl* (β_sexmale + (0.5 x β_genotype3k:sexmale)).

Cluster Markers identification

Seurat function “FindAllMarkers” was used with test.use = "wilcox" to find cluster markers for both midbrain neurons and microglia datasets.

Cluster Composition

Cluster composition was calculated for genotypes per cluster, using Generalized Linear Models (GLM: quasibinomial) on sample-level proportions. Adjusted p-values for multiple comparisons across clusters were calculated using Benjamini–Hochberg method. Given the limited number of biological replicates (n = 2 per genotype) and the resulting wide 95% CIs encompassing the null value (OR = 1), these results should be interpreted cautiously, with emphasis on effect sizes (ORs) and the precision of their estimates (95% CIs), alongside sample-level variation rather than statistical significance.

Gene Ontology (GO) and Gene set Enrichment (GSEA) analysis

For GO analysis, the R package “enrichR” version ‘3.4’ was used with these databases: "GO_Biological_Process_2025", "GO_Molecular_Function_2025", "GO_Cellular_Component_2025", "KEGG_2019_Mouse", "WikiPathways_2024_Mouse", "BioPlanet_2019". The significantly (adjusted p-value < 0.05) up and down- regulated genes from the pseudobulk DE analysis (*3K*^{het} vs *Ctrl*) were used as input gene lists. For GSEA analysis (Subramanian 2005: https://doi.org/10.1073/pnas.050658010),

“fgsea” package version 1.32.4.[57], and “msigdbr” version 25.1.1 were used for gene set enrichment analysis with these MSigDB collections: Hallmark (H), Canonical Pathways (C2:CP), GO Biological Process (C5:GO:BP), GO Molecular Function (C5:GO:MF), GO Cellular Component (C5:GO:CC), WikiPathways (C2:CP:WIKIPATHWAYS), KEGG Legacy Pathways (C2:CP:KEGG_LEGACY), and KEGG Medicus Pathways (C2:CP:KEGG_MEDICUS). For input a ranked gene list based on Wald statistic z from the pseudobulk DE analysis (*3K*^{het} vs *Ctrl*) was generated. The function “fgseaSimple” was run with these parameters: scoreType = "std", minSize = 5, maxSize = 500, nperm = 100000.

Differential cell communication network analysis

NATMI source code from the master branch, commit: f35f677, commit date: 2021-04-13, which is based on connectomeDB2020, was used to study changes in cell communications between *3K*^{het} and *Ctrl* in selected cell types [29]. For NATMI delta networks, the important stability criterion is that cell-type proportions within each condition/genotype are similar, i.e., microglia / neuron ratio (*3K*^{het}) ≈ microglia / neuron ratio (*Ctrl*). Neuron subtypes were defined as non-mDA, SNpc (Sox6 + TER), and VTA (excluding “unassigned”). Microglia subtypes were defined as immune cells (clusters 9 + 6), DAMs (clusters 3 + 8), and microglia (other clusters). To maintain a balanced cell type proportions within either genotype (dataset), stratified down-sampling was done independently for *Ctrl*-neurons and *3K*^{het}-neurons datasets at the granularity level determined by the predicted_Neighborhood, as well as for *3K*^{het}-microglia dataset at resolution 0.9, before merging the individual datasets based on genotype into separate control and *3K*^{het} datasets. For each merged dataset, a metadata column was created with unified ID prefixes “Nr_” for neurons and “Mg_” for microglia. To assign cell-type IDs, “pooled_TER” and “Seurat_clusters” were used for neuronal and microglial cell-types respectively. These assigned cell-types were used for annotations in the cell-label metafile, and normalized RNA assay was used to generate an expression matrix, both of which are required by NATMI. The annotations and expression matrix were saved as data tables for downstream analysis. The R package biomaRt (version 2.66.2) was used to generate a mouse-to-human ortholog mapping based on Ensembl release 115. Gene symbols detected in the expression matrices from both *Ctrl* and *3K*^{het} datasets were pooled and used as the query set. Only genes with a unique one-to-one mouse–human ortholog relationship were retained, and duplicate mouse or human gene mappings were removed. The resulting canonical mapping was saved as an RDS file and subsequently used to convert mouse gene symbols in the expression matrices to their corresponding human orthologs. NATMI’s “ExtractEdges” was run separately on *Ctrl* and *3K*^{het} datasets with interaction database (interDB) set to lrc2p. To identify the changes in ligand-receptor edge weights per cell-type between *Ctrl* and *3K*^{het}, NATMI’s “DiffEdges” was run with interDB = lrc2p, weightType = mean, ref = *Ctrl*, target = *3K*^{het}. Next, the output files “Up-regulated_mean.csv” (edges with higher expression weights in the target dataset), and “DOWN-regulated_mean.csv” (edges with lower expression weights in the target dataset) were used as input to create the network plots as well as the heatmaps. The exact workflow can be found at the Perlmann Lab GitHub page: https://github.com/xxx/.

PLX3397 treatment

Pexidartinib (PLX3397) was formulated in SDS_CRM standard chow at 290 mg/kg by SAFE Nutrition Service. PLX3397 diet was administered ad libitum for 5 weeks to *3K*^{het} and control littermates (n = 14–16) to deplete microglia and followed by a 5-week repopulation period with normal food. A control cohort (*3K*^{het} and controls, n = 12–14) was administered normal food at the same time (depletion and repopulation period) and used for behavioural assessment. Animals (n = 3 per group) were collected at the end of PLX3397 treatment and at the end of repopulation period and used for immunohistochemistry.

Behavioural tests

The sample size of each genotype × treatment × sex combination was *n* = 6–9 during the treatment phase, and *n* = 5–7 during the repopulation phase. Two animals (female 3K mice on PLX3397 treatment) with unilateral micropthalmia were excluded from the challenging beam traversal test due to the potential confounding effects of visual impairment on this test. Behavioural assessments were performed at week 7 (age of animal, before start of treatment) and at week 10, 12 (end of treatment), 14 and 17 (end of repopulation, see Fig. 5a), following known time points for depletion and repopulation of microglia with PLX3397 treatment [35]. The behavioural tests were conducted during the stated week, avoiding more than one test per day. Beam-traversal performance and tremor were analyzed using linear mixed-effect models (lme4/lmerTest packages in R) with genotype, treatment, sex and week and their interactions as fixed effects, and a random intercept for animal. The tremor model additionally included body weight and recording box as covariates. Overall effects were assessed with Type III F-tests using Kenward-Roger-approximated degrees of freedom. Pairwise comparisons of estimated marginal means were used to test the treatment effect within each genotype × sex combination. To test whether treatment effects reversed following cessation at week 12, models were fit incorporating piecewise linear time terms that allow for different slopes for the on-treatment (weeks 7–12) and off-treatment (weeks 12–17) periods. The difference in slopes between the treatment groups was compared for the on- and off-treatment periods for each genotype × sex group, with Holm correction applied across comparisons.

Rotarod

Animals were tested for motor performance on a mouse rota-rod (Ugo Basile, 47600) at stated time intervals. All mice were pre-trained on the apparatus for 2 consecutive days at constant speed 5 rpm for 3 minutes before the first trial. The test was conducted at accelerating speed (4–40 rpm) over 5 minutes for 3 consecutive trials, with a 10 min rest period between trials to reduce stress and fatigue.

Tremor

Tremor was recorded using the Tremor Monitor system and software (San Diego Instruments, San Diego, CA, USA). Prior to the first recording timepoint, mice underwent a single 10 min habituation session in the apparatus without data collection. At each testing timepoint, mice were placed inside an accelerometer-mounted cylindrical Plexiglas enclosure (12.7 cm [L] x 3.8 cm [I.D.]) within a recording chamber for 10 min. The first 5 min served as an acclimatization period, while recordings were taken

during the subsequent 5 min. Whole-body movement was transduced by the accelerometer and digitized at a sampling rate of 128 Hz. The resulting signal was passed through a Fast Fourier Transform to yield a frequency spectrum, and a tremor score was derived from the area under the curve (AUC) of the 10–14 Hz band, the frequency range characteristic of tremor in 3K mice, as determined by prior pilot studies.

Challenging beam traversal test

Fine motor coordination and balance were assessed using a modified challenging beam traversal test[58]. The apparatus consisted of a 1-meter-long Plexiglas beam with four segments of decreasing width (3.5 cm, 2.5 cm, 1.5 cm and 0.5 cm). The beam was elevated 15 cm above the bench and led to the animal's home cage at the narrow end, serving as the goal. The testing room was brightly lit (approx. 500 lux), while the home cage was partially covered to provide lower lighting (approx. 150 lux) to further motivate mice to traverse the beam. Mice were trained on two consecutive days, performing four practice crossings on each day on the flat surface of the beam. At testing timepoints, a metal mesh grid (0.5 x 0.5 cm) was placed 0.5 cm above the flat surface of the beam, increasing the demand on motor coordination and enabling measurement of the number of paw slips through the mesh grid. At each test timepoint, four crossings were recorded per animal, with the first crossing excluded and the remaining three averaged for analysis. Trials were video-recorded and scored in slow motion (0.25x speed) for time to cross the beam and number of paw slips.

Use of Large Language Models (LLMs)

OpenAI-ChatGPT4 was used to improve language quality and check grammar of the original text that was generated by authors. All output was reviewed, edited and verified by the authors, who take full responsibility for the content.

Results

3K-hα-syn **accumulates in ventral midbrain regions adjacent to dopamine neurons and is accompanied by microgliosis**

To characterise the distribution of the Thy1-driven 3K-hα-syn protein within the ventral midbrain, we performed immunohistochemical analysis of six-month-old *3K* heterozygotes (*3K*^{het}) and control littermate mice using antibodies against hα-syn and α-syn phosphorylated at serine 129 (pα-syn). Immunoreactivity for both hα-syn and pα-syn was virtually absent from tyrosine hydroxylase (TH)-positive mDA neurons (Fig. 1A,B). Instead, robust signals for hα-syn and pα-syn were detected in an adjacent, non-dopaminergic midbrain territory, most prominently in the red nucleus (Fig. 1A,C). In control littermates hα-syn and pα-syn immunoreactivity were undetectable under the same imaging conditions, in accord with their human specificity (Fig. 1A). These findings demonstrate that, in the 3K-hα-syn model, pathological accumulation at six months is prominent in non-dopaminergic neurons of the ventral midbrain rather than in the mDA neurons themselves. The lack of expression in mDA neurons is consistent with previous reports of a transgenic model using Thy1 promoter-driven α-syn pathology [25,26].

However, when the 3K-hα-syn model was originally developed, dot-like accumulation of hα-syn could be noted in some TH+ cells in the SNpc [8]. We were unable to detect any such accumulation. The discrepancy between this and the current study could be due to genetic drift in the 3K-hα-syn model or other methodological differences.

Despite the absence of prominent accumulation of 3K-hα-syn in mDA neurons, the presence of pathological pα-syn in the adjacent regions suggested a broader neuroinflammatory reaction. Immunohistochemistry for the pan-microglial marker Iba1 revealed increased microglial density and altered morphology in the ventral midbrain of six-months old *3K^{het}* mice compared to controls (Fig. 1D). To quantify this response, we performed flow cytometric analysis of CD45 + ventral midbrain immune cells. This analysis confirmed a significant elevation of CD45 + cells in *3K^{het}* mice relative to controls (n = 5 per group, $p < 0.05$; Fig. 1E), establishing that a robust neuroinflammatory response accompanies the 3K-hα-syn pathology in this region.

A) Immunohistochemistry (IHC) for human alfa-synuclein (hα-syn) and phospho alfa-synuclein S129 (pα-syn) in 6 months old ventral midbrain of *3K^{het}* and control mice. B-C) Close-ups of the boxed areas shown in A). D) Immunohistochemistry for TH and general microglial marker Iba1 in the ventral midbrain of 6 months old *3K^{het}* and control animals. E) Quantification result of Cd45^{+} immune cells by FACS from the ventral midbrain tissue of 6 months old *3K^{het}* (n = 5) and control (n = 5). * $p < 0.05$. Unpaired t-test. Tiled images in A, D. Scalebars 500 um in A, D, 50 um in B, C.

Single-nucleus RNA sequencing reveals upregulation of cholesterol biosynthesis and downregulation of synaptic gene programmes in 3K^{het} mDA neurons

Although mDA neurons in *3K^{het}* mice showed no detectable accumulation of hα-syn, we hypothesized that their pathological and inflammatory environment could still influence the transcriptional state of these neurons. To investigate this possibility, we performed single-nucleus RNA sequencing (snRNAseq) of mDA neurons from 4–5 months old *3K^{het}* and control mice (Fig. 2A). To enable enrichment of mDA nuclei by FACS, we used a nuclear fluorescent tagging strategy, crossing *3K^{het}* mice with mice harbouring *Slc6a3^{Cre}* and nuclear mCherry-encoding *TrapC^{flox}* alleles (Fig. 2A). Following sequencing and bioinformatic analysis, mDA nuclei were resolved into seven transcriptionally distinct subpopulations corresponding to the previously defined mDA neuron territories (subtypes) [27] – *Ebf1, Fbn2, Gad2, Pdia5, Pcsk6, Otx2*, and *Sox6* (Fig. 2B, Supplementary Fig. 1, Supplementary Table 1; also in agreement with Gaertner et al. [28]).

UMAP visualisation and comparison of cell distributions between genotypes revealed that control and *3K^{het}* nuclei were broadly intermingled across all clusters (Fig. 2C), with no significant shift in the relative proportions of any mDA subpopulation between the two genotypes (quasibinomial generalised linear model, see Methods; Fig. 2D, Supplementary Table 2). This indicates that exposure to the inflammatory microenvironment does not alter the overall transcriptional identity or subtype architecture of the mDA

neuron population at this age. Nevertheless, differential expression analysis identified a number of genes reaching significance (adjusted $p < 0.05$, abs(log2FC) > 0.3) (Fig. 2E, Supplementary Table 3).

Differentially expressed genes included the upregulation of Nfe2l2, a master regulator of antioxidant response, together with *Ldlr, Fdft1* and *Srpx*, consistent with activation of oxidative stress and lipid metabolic pathways in *3K*^{het} mDA neurons (Fig. 2E). Gene set enrichment analysis identified cholesterol and sterol biosynthesis among the significantly upregulated pathways (Fig. 2F, Supplementary Table 4), indicating a coordinated metabolic response.

A) A schematic showing the approximate region of the midbrain from where immune cells and mDA nuclei were collected for sorting and sequencing. B) UMAP plot of all cells in the mDA dataset, both from *3K*^{het} and control, colour coded for different mDA subclusters. C) UMAP plot showing the distribution of control and *3K*^{het} cells in the dataset. D) Mean territory proportions per sample across the clusters (territories) between *3K*^{het} and control, calculated using a quasibinomial GLM. For all comparisons, 95% CI encompass the null value OR = 1 (n = 2 samples per genotype). E) A volcano plot showing selected significantly different (adj.p-value < 0.05, abs(log2FC) > 0.3) genes between *3K*^{het} and control neurons. UP=higher expression in *3K*^{het}, DOWN=lower expression in *3K*^{het}. F) GSEA Wikipathways with significant differential enrichment in *3K*^{het} neurons compared to control. logPadj = -log10(adjusted p-value). G) GO-terms for biological processes that were significantly up- or downregulated in *3K*^{he} compared to the control.

In contrast, *Prkn* expression was modestly reduced, and Gene Ontology analysis revealed significant downregulation of neuronal and synaptic processes (Fig. 2G, Supplementary Table 5). Together with reduced expression of the activity-dependent transcription factor *Egr1*, these findings suggest that mDA neurons undergo a modest but significant transcriptional shift away from neuronal function and toward lipid dysregulation and stress adaptation while retaining their overall subtype integrity.

CD45 + midbrain immune cells in 3K^{het} mice transition to a DAM state with upregulation of neurodegeneration-associated gene programmes

Next, using single-cell RNA sequencing (scRNAseq) of CD45 + FACS-isolated immune cells from the ventral midbrain of *3K*^{het} and control animals at age 5–6 months (Fig. 2A) we characterised the microglial response in greater depth. After dimensionality reduction and semi-supervised clustering, marker gene expression identified transcriptionally distinct cell populations: homeostatic microglia, proliferating microglia, DAM, and monocytes/macrophages (Fig. 3B,C, Supplementary Table 6). UMAP visualisation showed a marked asymmetry in the distribution of cells between genotypes, with several clusters populated almost exclusively by *3K*^{het}-derived cells (Fig. 3A, highlighted regions). Quantitative analysis of cluster proportions confirmed that clusters 3 and 8, corresponding to DAM populations, showed large estimated increases in *3K*^{het} mice relative to controls (Odds Ratio (OR) = 5.65 and 7.04, respectively), while homeostatic microglial clusters 0 and 1 were correspondingly mildly depleted with

OR = 0.85 and 0.6, respectively using a quasibinomial generalised linear model. However, the 95% CIs were very wide and included the null value (OR = 1). Given the low number of biological replicates (n = 2 per genotype), these estimates have limited statistical power and should therefore be interpreted as evidence of a potential enrichment of clusters 3 and 8 rather than definitive evidence; Supplementary Fig. 2A, B, Supplementary Table 7.

Examination of the marker gene profile of the *3K*^{het}-enriched clusters revealed strong upregulation of canonical DAM genes including *Apoe, Lgals3* (Galectin-3), *Fabp5, Spp1, Clec7a, Cst7, Lpl*, and *Mmp12*, with the expression of *Apoe* and *Lgals3* clearly localised to the *3K*^{het}-enriched regions of the UMAP (Fig. 3C-E; Supplementary Fig. 2C). Differential gene expression analysis, further highlighted *Apoe* as one of the most significantly and strongly upregulated genes in *3K*^{het} immune cells, alongside *Fabp5, Lgals3, Clec7a*, and *Igf1* (Fig. 3D, Supplementary Table 8). The homeostatic microglial clusters, by contrast, showed lower expression of genes associated with synaptic pruning, amyloid-beta clearance, microglial cell activation, and antigen presentation, consistent with a loss of homeostatic functions in the context of the activated DAM phenotype (Supplementary Fig. 2D, Supplementary Table 9).

Pathway analysis of genes upregulated in *3K*^{het} immune cells by KEGG annotation identified neurodegeneration- and inflammation-associated gene expression, including significant enrichment of terms related to Parkinson disease, Alzheimer disease, oxidative phosphorylation, ribosome biogenesis, Toll-like receptor signalling, TNF signalling, and IL-17 signalling (Fig. 3F). Complementary GSEA analysis using Hallmark gene sets confirmed upregulation of TNFα signalling via NF-κB, interferon-gamma response, cholesterol homeostasis, inflammatory response, oxidative phosphorylation, and MYC target programmes (Fig. 3G, Supplementary Table 10). Together, these data indicate that the microglial response in the 3K-hα-syn model constitutes a shift to a disease-associated state characterised by the hallmark transcriptional signature of DAM, accompanied by induction of inflammatory, metabolic, and neurodegeneration-linked gene programmes.

A) UMAP plot showing the distribution of control and *3K*^{het} cells in the dataset. Encircled areas of the UMAPs highlight the area containing mostly *3K*^{het} cells. B) UMAP plot showing ten clusters of the dataset corresponding to monocytes, macrophages, and different types of microglia. C) A dot plot of selected genes enriched in the different clusters, together with general microglial marker genes. D) A volcano plot depicting selected genes either up- or downregulated (adj.p-value < 0.05, abs(log2FC) > 0.3) in *3K*^{het} immune cells compared to control. E) The expression of *Apoe* and *Lgals3* plotted on the UMAP. F) Significantly upregulated KEGG pathway terms in *3K*^{het} t immune cells. G) The significantly upregulated GSEA Hallmark pathways in *3K*^{het} immune cells.

Galectin-3 expression marks a progressive and region-restricted microglial activation

Having established the DAM identity of activated microglia in the midbrain of the *3K*^{het} mice at 6 months, we characterised the temporal dynamics of microglial activation as hα-syn pathology progressed in this model. We used Galectin-3 (Gal3), one of the most significantly upregulated DAM markers identified in our scRNAseq analysis, as a histological readout of DAM accumulation in the ventral midbrain. Immunohistochemistry was used to compare the distribution of Gal3 to that of pα-syn across the ventral midbrain from one to six months old mice (Supplementary Fig. 3).

At one month of age, pα-syn immunoreactivity was already detectable in the red nucleus of *3K*^{het} mice. This is before behavioural phenotypes have developed indicating that pathological α-syn cytoplasmic accumulation is an early event in this model [8]. Some Gal3 + microglia were also detected at this stage, suggesting the initiation of the DAM response. Gal3 immunoreactivity increased with age, with the signal mainly localising near pα-syn+ cells, particularly in the more posterior midbrain. However, these cells also infiltrated into the region where mDA neurons reside. At six months, Gal3 + microglia were abundant throughout the ventral midbrain of *3K*^{het} animals, with a pronounced signal in posterior regions, reflecting the spatial distribution of pα-syn.

In contrast, both pα-syn and Gal3 were virtually undetectable in six-month-old control animals (Supplementary Fig. 3). These observations establish that the DAM response in the *3K*^{het} mice is temporally and spatially coupled to the distribution of α-syn pathology, and that it starts already in very young animals.

pα-syn, Gal3, and Iba1 were further analysed across the entire brain in 6 months old *3K*^{het} and control animals. pα-syn was broadly expressed in different brain regions, while Iba1 and Gal3 were more prominent in caudal regions of the *3K*^{het} brain (Supplementary Fig. 4A). In addition to the high expression detected in the red nucleus, particularly high Iba1 and Gal3 signals were observed in medulla (Supplementary Fig. 4B,C). However, several other brain regions expressing high levels of pα-syn, such as subiculum and pontine nuclei, contained almost no Gal3 (Supplementary Fig. 4D,E). These results indicate that specific neuronal populations in the midbrain and hindbrain are more sensitive to pα-syn-mediated neuronal stress, which in these regions triggers microgliosis and the presence of DAMs.

Differential cell communication network analysis of midbrain mDA neurons and CD45 + immune cells show a homeostatic-to-DAM transition in 3K^{het} mice.

To investigate a potential for altered signalling between different cell populations in the *3K*^{het} ventral midbrain, we applied NATMI to transcriptomic profiles of SNpc and VTA mDA neurons, non-mDA neurons, microglia, DAMs, and other immune cells. NATMI infers directional communication from the expression of curated ligand-receptor pairs [29]. Expression weights reflect the abundance of the ligand in the sender and receptor in the receiver, whereas specificity weights indicate how selectively the two genes are expressed by the respective cell populations (Fig. 4A, B, Supplementary Fig. 5A, B).

Networks at the cell-type level revealed widespread increases in expression-weighted communication in *3K*^{het} mice, with the strongest change occurring in predicted immune-cell autocrine signalling (Fig. 4A,B). Some microglia-DAM interactions nevertheless showed reduced specificity (Fig. 4B), suggesting that ligand and receptor induction was shared across several cell populations rather than restricted to a single cellular route.

Analysis of individual ligand-receptor pairs identified a potential for increased APOE signalling from microglia to SNpc and VTA neurons through several lipoprotein receptors, including LDLR, LRP1, LRP8, VLDLR, SORL1, and SCARB1 (Figs. 4C,D). This is consistent with altered lipid transport and uptake during the neuroinflammation driven by expression of mutant (3K) α-syn. Additional changes indicated increased DAM to neuron IGF1-IGF1R signalling [30], immune-cell/DAM ADAM15-integrin interaction [31], and neuron to microglia GAS6-AXL signalling [32,33](Figs. 4C,D). These pathways may contribute to neuronal survival, cell adhesion, and regulation of microglial activation. Conversely, a potential for reduced CX3CL1-CX3CR1 signalling was consistent with the transition from homeostatic microglia to DAMs [14]. Indication of reduced SEMA4D-PLXNB2 and TR-TFRC signalling potentially reflects altered inflammatory regulation and response to reactive oxygen species [34] (Supplementary Fig. 5C, D, Supplementary Table 11). Together, these results indicate remodelling of neuron-immune communication in the *3K*^{het} midbrain, involving lipid metabolism, trophic signalling, immune activation, and stress responses.

A-B) Changes in cell interaction networks between *3K*^{het} and control among cell-types measured in ligand-receptor (LR) expression weights (A) and LR specificity weights (B), calculated as log2FC, based on a set of edges (LR pairs) with higher expression weights in the target dataset (3K). C-D) Heatmaps of log2FC (*3K*^{het}/Ctrl) of expression (C) and specificity (D) edge weights for the top 5 LR pairs in Log2FC edge expression weight per cell-type pair. Selection was done based on Log2FC edge expression weight and the same LR pairs were plotted for specificity. LR = Ligand-Receptor, red = higher in *3K*^{het}, blue = higher in control. Arrows: biological direction from sender (ligand-expressing) → receiver (receptor-expressing), arrow thickness indicates the interaction magnitude.

Pharmacological microglial depletion indicates a neuroprotective role of microglia in female 3K^{het} mice

As demonstrated above, the *3K*^{het} mice develop a robust DAM response within the ventral midbrain. To address whether microglia are functionally beneficial, detrimental, or neutral with respect to disease phenotypes, we pharmacologically depleted microglia using PLX3397, a potent inhibitor of Colony-Stimulating Factor 1 Receptor, CSF1R [35]. *3K*^{het} mice and control littermates were fed PLX3397-supplemented chow (290 mg/kg) for a 5-week depletion phase (weeks 7–12 of age), followed by a 5-week repopulation period on normal diet (weeks 12–17), with parallel control groups (non-transgenic and *3K*^{het} mice) maintained on normal diet throughout the different treatment phases (Fig. 5A). Motor behaviour using the beam traversal, rotarod, and tremor assays was assessed at multiple time points covering the baseline, depletion, and repopulation phases (Fig. 5A).

At the end of the depletion phase at week 12, PLX3397 treatment produced a dramatic reduction in both Iba1 + microglial and Gal3 + DAM signal in the ventral midbrain (Fig. 5B). Quantification of Iba1 and Gal3 immunoreactivity revealed a significant depletion of regular microglia and DAM in both *3K*^{het} and control animals on PLX3397 diet compared to the normal diet (one-way ANOVA with Tukey post-hoc, $p < 0.001$ for both comparisons; Fig. 5C,D, Supplementary Table 12). Some Gal3 + microglia were already present in the *3K*^{het} ventral midbrain before the onset of PLX3397 treatment, establishing that the DAM response precedes the pharmacological depletion (Supplementary Fig. 6A). After the 5-week repopulation period, Iba1 + and Gal3 + microglia had repopulated the ventral midbrain in both PLX3397-treated groups (Supplementary Fig. 6B).

A) Schematic of the depletion plan, with timepoints of behavioral testing indicated with blue triangles. B) Representative IHC stainings for Iba1 and Gal3 of *3K*^{het} and control midbrains, fed either normal or PLX3397-supplemented diet, after the 5-week depletion phase. The left panel shows the overlay of Iba1, Gal3, and DAPI, and the right panel shows Gal3 and DAPI only. Scalebars 100 um. C-D) Quantification of Iba1^{+} and Gal3^{+} signal per area. N = 3 for each group. *** $p < 0.001$, ** $p < 0.01$, *$p < 0.05$. One-way ANOVA with Tukey. E) Beam test result divided by sex and genotype. Upper part depicts the time to cross and lower part depicts the slope difference between treatment and control groups. Blue background indicates depletion phase, and white background indicates repopulation phase. n = 4–6 per group *** $p < 0.001$, *$p < 0.05$ 4-way repeated measures ANOVA. NTG, non-transgenic (control) animal.

PLX3397-treatment did not affect the behaviour of *3K*^{het} mice in either the rotarod test or tremor assay (Supplementary Fig. 7A-C, Supplementary Table 13). However, the beam traversal test revealed a striking, sex-specific effect of microglial depletion on motor performance (Fig. 5E, Supplementary Table 14). During the depletion phase, time to cross the beam increased by an average 1.03 s/week for *3K*^{het} females on PLX3397 diet compared to 0.38 s/week on normal diet, an additional worsening of 0.65 s/week attributable to the PLX3397 diet (95% CI 0.34 to 0.96, $p < 0.001$). This effect reversed during the repopulation phase, with a net improvement of 0.54 s/week relative to the control (95% CI -0.87 to -0.22, $p = 0.001$). The change in PLX-control slope difference between depletion and repopulation phases was itself also significant (-1.19 s/week, 95% CI -1.74 to -0.64, $p < 0.001$), confirming that the detrimental effect resolved after cessation of PLX3397 treatment. This pattern was specific to *3K*^{het} females, as neither non-transgenic females nor males of either genotype showed a significant slope difference between PLX3397 and normal diet in either phase. These results indicate a protective function of microglia in beam traversal performance specifically in female *3K*^{het} mice, suggesting that the neuroinflammatory response in this model is at least partly adaptive rather than purely deleterious.

Discussion

The present study provides a comprehensive characterization of the neuronal and immune responses within the ventral midbrain of the *3K*^{het} mouse model. We used complementary histological analyses, single-cell transcriptomics and pharmacological depletion of microglia to investigate the consequences

of 3K-hα-syn-induced pathology. Several observations are notable. First, at six months 3K-hα-syn and pα-syn were essentially undetectable in TH-positive mDA neurons. In contrast, 3K-hα-syn and pα-syn accumulated in adjacent non-dopaminergic regions, most prominently in red nucleus neurons. Second, extensive microgliosis, associated with transition into a DAM transcriptomic profile, was seen in the region of the red nucleus but also extended into the regions with mDA neurons as evidenced by expression of Gal3. Third, pharmacological depletion of microglia with the CSF1R inhibitor PLX3397 selectively worsened beam-traversal performance in female *3K^{het}* mice, indicating that microglia are not purely deleterious in this model.

The selective high expression of 3K-hα-syn in red nucleus neurons creates a setting in which mDA neurons are localized in proximity to regions associated with extensive microgliosis, including DAM. Activated microglia were also observed within the region where mDA (i.e, TH+) neurons are localized within the SNpc and VTA. Thus, although we cannot exclude a low level of undetectable 3K-hα-syn, the transcriptional changes we detected in mDA neurons are an indication of a prominent non-cell-autonomous effect of the neighbouring pathology and of the associated microglia-mediated inflammatory response.

Our snRNAseq analysis showed that the previously defined mDA neuron subtypes were all present in *3K^{het}* mice [27], and that the subtype proportions were preserved in 4–5-month-old *3K^{het}* mice, with no evidence of subtype-selective loss or transition towards a degenerative transcriptional state. However, differential expression analysis identified a limited number of genes, including upregulation of *Nfe2l2, Ldlr, Fdft1* and *Srpx*, enrichment of cholesterol and sterol biosynthesis pathways, and a coordinated downregulation of synaptic and neuronal gene ontology terms together with reduced *Egr1*, driving activity-dependent gene expression and a modest reduction in *Prkn*, known to be mutated in autosomal recessive PD and implicated in mitochondrial quality control pathways [36,37]. Thus, although these effects are relatively small, and none of the changes have yet been corroborated at the protein level, a plausible conclusion is that these transcriptional trends reflect a coherent shift from neuronal function towards stress adaptation and lipid handling as a response to an α-syn-driven inflamed environment.

In contrast to the relatively modest transcriptional changes in mDA neurons, the transcriptional change of microglia was robust as evidenced from scRNAseq analysis of CD45 + cells transitioning into DAM in *3K^{het}* mice. The *3K^{het}* DAM expressed the canonical DAM signature (*Apoe, Lgals3, Fabp5, Spp1, Clec7a, Cst7, Lpl, Mmp12*), with reciprocal reduction of homeostatic gene programmes and enrichment of TNF, interferon-gamma, Toll-like receptor and oxidative phosphorylation pathways. One of the most intriguing findings in this study is the convergence of neuronal and microglial transcriptional changes on cholesterol metabolism, suggesting that lipid homeostasis may represent an interface through which activated microglia influence neurons exposed to α-syn-mediated pathological stress. Expression analysis showed that microglia strongly induce Apoe while mDA neurons show a modest increase in several lipoprotein receptors. In parallel, differential cell communication network analysis using NATMI predicted enhanced APOE interactions from microglia to neurons. Although these predictions require experimental validation, the convergence of neuronal transcriptomics, microglial transcriptomics and

ligand-receptor analysis suggests a coordinated remodelling of lipid metabolism in the ventral midbrain. Increasing evidence suggests that α-syn aggregation can lead to disturbances of lipid homeostasis, membrane dynamics, vesicular trafficking and neuroimmune signalling, leading to the view that PD, in part, is a disorder of lipid biology [38–41]. Future studies will be required to determine whether such metabolic changes primarily support neuronal survival or if they contribute to disease progression.

The identified DAM transcriptional response was histologically confirmed and investigated both in the midbrain and other regions of the mouse brain. The temporal analysis in the ventral midbrain demonstrated the presence of Gal3 + DAM already at one month of age, before any behavioural phenotype is evident, indicating that DAM induction is an early rather than a late event. In addition, the *Thy1* promoter used to drive 3K-hα-syn expression results in a broad but non-uniform neuronal expression [25], and our histological examination identified strong 3K-hα-syn in the red nucleus but also in other regions of the brain. In addition to the red nucleus, pα-syn was highly expressed in several brain regions, e.g. in the subiculum and pontine nuclei; however, Iba1 and Gal3 were particularly prominent in caudal regions of the *3K^{het}* brain. Thus, these observations point to a differential sensitivity to 3K-hα-syn that appears to trigger an inflammatory response around sensitive neuron populations while other regions with a heavy pα-syn burden appear resilient. This could depend on the properties of the affected neurons, the local microglia, or both. Regional heterogeneity of microglia has been documented before [42,43] (reviewed in ref. 42), and identifying determinants of this selective vulnerability is an important question that warrants further investigation.

A powerful experimental approach to dissect the causal role of microglia is the pharmacological depletion of these cells using small-molecule inhibitors of CSF1R [35,44]. A notable finding in our study was that the CSF1R inhibitor, PLX3397, which efficiently depleted Iba1 + and Gal3 + cells, clearly slowed beam-traversal crossing in female *3K^{het}* mice, thus worsening a behavioural phenotype. The PLX3397-dependent beam-traversal phenotype was absent in males and in non-transgenic mice and stabilised in females upon microglial repopulation. Neuroinflammation involving microglia is a defining feature of PD neuropathology[10]. Post-mortem studies and PET imaging suggest that sustained microglial reactivity can contribute to mDA neurodegeneration in the SNpc [11,12]. Our data indicate a beneficial effect of microglia in this model (at least in females), which contrasts with several previous studies in α-syn models in which CSF1R-mediated microglial depletion appears to confer neuroprotection. However, the literature has remained inconsistent, with reports describing beneficial, neutral or detrimental consequences of microglial depletion [19–21,45]. Such discrepancies likely reflect differences in α-syn models, disease stage, timing of depletion and other variables. DAM may be protective, e.g. by contributing to increased neuronal maintenance by clearing pathological tissue debris, limiting inflammatory spread or providing trophic support [10]. It is also becoming increasingly understood that DAM are heterogeneous populations whose functions depend on disease stage and pathological context. Thus, it seems likely that microglia may be predominantly protective during early disease, which is consistent with the experimental design of this study, but that a transition toward increasingly pro-pathological inflammation occurs at later stages of disease [46].

The sex-specific behavioural phenotype noted here is intriguing. Parkinson's disease incidence is lower in women, and increasing evidence indicates fundamental sex differences in microglial development and immune responsiveness [23,24,47]. Our findings suggest that in certain contexts, female microglia may provide protection rather than harmful inflammatory stress. Indeed, our data are consistent with previous transcriptomic studies showing that adult female microglia adopt a comparatively homeostatic or reparative phenotype, whereas male microglia exhibit greater enrichment of inflammatory pathways [23,24]. These differences are not generally observed and are likely context dependent. Whether this reflects hormonal influences, intrinsic differences in microglial state, or differences in neuron-glia interactions remains unresolved. Future studies focused on transcriptomic differences between males and females in developing and mature microglia may help to identify mechanisms underlying sex-dependent differences as those seen here.

Conclusions

Together, our findings provide new insight into α-syn-mediated pathology, neuronal adaptation, and microglial activation during early stages of α-syn pathology. The findings indicate neuron-microglia signalling responses that include lipid and other metabolic remodelling and support the view that immunomodulatory therapies for PD may require selective targeting of specific microglial states rather than general suppression of neuroinflammation.

Abbreviations

3K-hα-syn: Human alpha-synuclein carrying the E35K, E46K and E61K substitutions; α-syn: Alpha-synuclein; pα-syn: Alpha-synuclein phosphorylated at serine 129; ANOVA: Analysis of variance; AUC: Area under the curve; CCA: Canonical correlation analysis; CD45: Cluster of differentiation 45; CI: Confidence interval; CSF1R: Colony-stimulating factor 1 receptor; DAM: Disease-associated microglia; DAPI: 4',6-Diamidino-2-phenylindole; DE: Differential expression; DMSO: Dimethyl sulfoxide; DPBS: Dulbecco's phosphate-buffered saline; FACS: Fluorescence-activated cell sorting; FBS: Fetal bovine serum; Gal3: Galectin-3; GLM: Generalised linear model; GO: Gene Ontology; GSEA: Gene set enrichment analysis; hα-syn: Human alpha-synuclein; HBSS: Hanks' balanced salt solution; HVG: Highly variable gene; Iba1: Ionised calcium-binding adaptor molecule 1; IHC: Immunohistochemistry; KEGG: Kyoto Encyclopedia of Genes and Genomes; L-Dopa: Levodopa; log2FC: Log2 fold change; LR: Ligand–receptor; mDA: Midbrain dopamine; MSigDB: Molecular Signatures Database; NATMI: Network Analysis Toolkit for Multicellular Interactions; NEBULA: Negative binomial mixed model using a large-sample approximation; NTG: Non-transgenic; OR: Odds ratio; PBS: Phosphate-buffered saline; PCA: Principal component analysis; PD: Parkinson's disease; PET: Positron emission tomography; PFA: Paraformaldehyde; QC: Quality control; RT: Room temperature; scRNAseq: Single-cell RNA sequencing; SNpc: Substantia nigra pars compacta; snRNAseq: Single-nucleus RNA sequencing; SNN: Shared nearest neighbour; SVD: Singular value decomposition; TBS: Tris-buffered saline; TH: Tyrosine hydroxylase; UMAP: Uniform manifold approximation and projection; VST: Variance stabilising transformation; VTA: Ventral tegmental area

Declarations

Ethics approval and consent to participate

All mouse experiments followed the guidelines and recommendations of Swedish animal protection legislation and were approved by Stockholm North Animal Ethics board (permit 16527-2023;8799-25; 3218-2022).

Consent for publication

Not applicable

Availability of data and materials

The datasets used and/or analysed during the current study are available from the corresponding author on reasonable request. The code for this study computational analyses can be found at the Perlmann Lab GitHub page: https://github.com/xxx/.

Competing interests

The authors declare that they have no competing interests.

Funding

We wish to thank Lexa/Nordstjernan for financial support to the Karolinska-Harvard Collaboration on Parkinson's Disease, the Swedish Research Council (2020_00884; 2025-02432), and Hjärnfonden (FO2023-0028).

Authors' contributions

TP, LL, IH, LG, BYS conceptualized the study and designed the experiments. SN and DS established the mouse model and advised on animal experiments. LG, IH, LL, and NB performed the experiments. BYS performed the computational analysis, data curation and deposition. LG, LL, BYS, and NB made the figures. TP, LG, BYS, IH, NB, and LL drafted the manuscript. All authors read the manuscript critically and revised it. TP, PS, DS, and SN secured funding.

Acknowledgements

The authors acknowledge the contributions of the Biomedicum Flow cytometry Core facility, financed by the Infrastructure Board at Karolinska Institutet, for providing access to equipment. The authors also acknowledge support from the National Genomics Infrastructure (NGI), SciLifeLab, Stockholm, Computational resources provided by the National Academic Infrastructure for Supercomputing in Sweden (NAISS), funded by the Swedish Research Council, for infrastructure support.

References

1. Poewe W, Seppi K, Tanner CM, Halliday GM, Brundin P, Volkmann J, Schrag A-E, Lang AE. Parkinson disease. Nat Rev Dis Prim. 2017;3:17013. https://doi.org/10.1038/nrdp.2017.13.
2. Armstrong MJ, Okun MS. Diagnosis and Treatment of Parkinson Disease. JAMA. 2020;323:548–60. https://doi.org/10.1001/jama.2019.22360.
3. Shahmoradian SH, Lewis AJ, Genoud C, Hench J, Moors TE, Navarro PP, Castaño-Díez D, Schweighauser G, Graff-Meyer A, Goldie KN, et al. Lewy pathology in Parkinson's disease consists of crowded organelles and lipid membranes. Nat Neurosci. 2019;22:1–17. https://doi.org/10.1038/s41593-019-0423-2.
4. Spillantini MG, Schmidt ML, Lee VM, Trojanowski JQ, Jakes R, Goedert M. Alpha-synuclein in Lewy bodies. Nature. 1997;388:839–40. https://doi.org/10.1038/42166.
5. Baba M, Nakajo S, Tu PH, Tomita T, Nakaya K, Lee VM, Trojanowski JQ, Iwatsubo T. Aggregation of alpha-synuclein in Lewy bodies of sporadic Parkinson's disease and dementia with Lewy bodies. Am J Pathol. 1998;152:879–84.
6. Braak H, Tredici KD, Rüb U, de Vos RAI, Steur ENHJ, Braak E. Staging of brain pathology related to sporadic Parkinson's disease. Neurobiol Aging. 2003;24:197–211. https://doi.org/10.1016/s0197-4580(02)00065-9.
7. Polymeropoulos MH, Lavedan C, Leroy E, Ide SE, Dehejia A, Dutra A, Pike B, Root H, Rubenstein J, Boyer R, et al. Mutation in the α-Synuclein Gene Identified in Families with Parkinson9s Disease. Science. 1997;276:2045–7. https://doi.org/10.1126/science.276.5321.2045.
8. Nuber S, Rajsombath M, Minakaki G, Winkler J, Müller CP, Ericsson M, Caldarone B, Dettmer U, Selkoe DJ. Abrogating Native alpha-Synuclein Tetramers in Mice Causes a L-DOPA-Responsive Motor Syndrome Closely Resembling Parkinson's Disease. Neuron. 2018;100:75–e905. https://doi.org/10.1016/j.neuron.2018.09.014.
9. Dettmer U, Newman AJ, Soldner F, Luth ES, Kim NC, von Saucken VE, Sanderson JB, Jaenisch R, Bartels T, Selkoe D. Parkinson-causing α-synuclein missense mutations shift native tetramers to monomers as a mechanism for disease initiation. Nat Commun. 2015;6:7314. https://doi.org/10.1038/ncomms8314.
10. Tansey MG, Wallings RL, Houser MC, Herrick MK, Keating CE, Joers V. Inflammation and immune dysfunction in Parkinson disease. Nat Rev Immunol. 2022;22:657–73. https://doi.org/10.1038/s41577-022-00684-6.
11. McGeer PL, Itagaki S, Boyes BE, McGeer EG. Reactive microglia are positive for HLA-DR in the substantia nigra of Parkinson's and Alzheimer's disease brains. Neurology. 1988;38:1285–1285. https://doi.org/10.1212/wnl.38.8.1285.
12. Gerhard A, Pavese N, Hotton G, Turkheimer F, Es M, Hammers A, Eggert K, Oertel W, Banati RB, Brooks DJ. In vivo imaging of microglial activation with [11C](R)-PK11195 PET in idiopathic Parkinson's disease. Neurobiol Dis. 2006;21:404–12. https://doi.org/10.1016/j.nbd.2005.08.002.

13. Blauwendraat C, Vallerga CL, Heilbron K, Bandres-Ciga S, Chang D, Tan M, Kia DA, Noyce AJ, Xue A, Young E, et al. Identification of novel risk loci, causal insights, and heritable risk for Parkinson's disease: a meta-analysis of genome-wide association studies. Lancet Neurol. 2019;18:1091–102. https://doi.org/10.1016/s1474-4422(19)30320-5.
14. Keren-Shaul H, Spinrad A, Weiner A, Matcovitch-Natan O, Dvir-Szternfeld R, Ulland TK, David E, Baruch K, Lara-Astaiso D, Tóth B, et al. A Unique Microglia Type Associated with Restricting Development of Alzheimer's Disease. Cell. 2017;169:1276–e129017. https://doi.org/10.1016/j.cell.2017.05.018.
15. Krasemann S, Madore C, Cialic R, Baufeld C, Calcagno N, Fatimy RE, Beckers L, O'Loughlin E, Xu Y, Fanek Z, et al. The TREM2-APOE Pathway Drives the Transcriptional Phenotype of Dysfunctional Microglia in Neurodegenerative Diseases. Immunity. 2017;47:566–e5819. https://doi.org/10.1016/j.immuni.2017.08.008.
16. Deczkowska A, Keren-Shaul H, Weiner A, Colonna M, Schwartz M, Amit I. Disease-Associated Microglia: A Universal Immune Sensor of Neurodegeneration. Cell. 2018;173:1073–81. https://doi.org/10.1016/j.cell.2018.05.003.
17. Butovsky O, Weiner HL. Microglial signatures and their role in health and disease. Nat Rev Neurosci. 2018;19:622–35. https://doi.org/10.1038/s41583-018-0057-5.
18. García-Revilla J, Venero JL, Rodríguez-Gómez JA. Galectin 3: A new player in the pathogenesis of Parkinson's disease. Neural Regen Res. 2025;21:1132–3. https://doi.org/10.4103/nrr.nrr-d-24-01410.
19. Lai TT, Kim YE, Nguyen LTN, Nguyen TT, Kwak IH, Richter F, Kim YJ, Ma H. Microglial inhibition alleviates alpha-synuclein propagation and neurodegeneration in Parkinson's disease mouse model. npj Park 's Dis. 2024;10:32. https://doi.org/10.1038/s41531-024-00640-2.
20. Bhatia TN, Jamenis AS, Abbas M, Clark RN, Miner KM, Chandwani MN, Kim RE, Hilinski W, O'Donnell LA, Luk KC, et al. A 14-day pulse of PLX5622 modifies α-synucleinopathy in preformed fibril-infused aged mice of both sexes. Neurobiol Dis. 2023;184:106196. https://doi.org/10.1016/j.nbd.2023.106196.
21. Stoll AC, Kemp CJ, Patterson JR, Kubik M, Kuhn N, Benskey M, Duffy MF, Luk KC, Sortwell CE. Alpha-synuclein inclusion responsive microglia are resistant to CSF1R inhibition. J Neuroinflammation. 2024;21:108. https://doi.org/10.1186/s12974-024-03108-5.
22. Iba M, Lee Y-J, Horan-Portelance L, Chang K, Szabo M, Rissman RA, You S, Masliah E, Kim C. Microglial and neuronal fates following inhibition of CSF-1R in synucleinopathy mouse model. Brain Behav Immun. 2025;123:254–69. https://doi.org/10.1016/j.bbi.2024.09.016.
23. Villa A, Gelosa P, Castiglioni L, Cimino M, Rizzi N, Pepe G, Lolli F, Marcello E, Sironi L, Vegeto E, et al. Sex-Specific Features of Microglia from Adult Mice. Cell Rep. 2018;23:3501–11. https://doi.org/10.1016/j.celrep.2018.05.048.
24. Guneykaya D, Ivanov A, Hernandez DP, Haage V, Wojtas B, Meyer N, Maricos M, Jordan P, Buonfiglioli A, Gielniewski B, et al. Transcriptional and Translational Differences of Microglia from Male and

Female Brains. Cell Rep. 2018;24:2773–e27836. https://doi.org/10.1016/j.celrep.2018.08.001.

25. van der Putten H, Wiederhold K-H, Probst A, Barbieri S, Mistl C, Danner S, Kauffmann S, Hofele K, Spooren WPJM, Ruegg MA, et al. Neuropathology in Mice Expressing Human α-Synuclein. J Neurosci. 2000;20:6021–9. https://doi.org/10.1523/jneurosci.20-16-06021.2000.
26. Vlcek B, Dumas S, Ekmark-Lewén S, Rubino E, Ingelsson M, Wallén-Mackenzie Å. Aldh1a1 and additional markers of dopamine cell heterogeneity in substantia nigra and ventral tegmental area identified as preserved in two transgenic α-synuclein mouse models of neurodegenerative disease. Explor Neuroprotective Ther. 2023;3:299–327. https://doi.org/10.37349/ent.2023.00053.
27. Salmani BY, Lahti L, Gillberg L, Jacobsen JK, Mantas I, Svenningsson P, Perlmann T. (2024). Transcriptomic atlas of midbrain dopamine neurons uncovers differential vulnerability in a Parkinsonism lesion model. eLife *12*, RP89482. https://doi.org/10.7554/elife.89482
28. Gaertner Z, Oram C, Schneeweis A, Schonfeld E, Bolduc C, Chen C, Dombeck D, Parisiadou L, Poulin J-F, Awatramani R. (2025). Molecular and spatial transcriptomic classification of midbrain dopamine neurons and their alterations in a LRRK2G2019S model of Parkinson's disease. eLife *13*, RP101035. https://doi.org/10.7554/elife.101035
29. Hou R, Denisenko E, Ong HT, Ramilowski JA, Forrest ARR. Predicting cell-to-cell communication networks using NATMI. Nat Commun. 2020;11:5011. https://doi.org/10.1038/s41467-020-18873-z.
30. Ueno M, Fujita Y, Tanaka T, Nakamura Y, Kikuta J, Ishii M, Yamashita T. Layer V cortical neurons require microglial support for survival during postnatal development. Nat Neurosci. 2013;16:543–51. https://doi.org/10.1038/nn.3358.
31. Hsia H-E, Tüshaus J, Brummer T, Zheng Y, Scilabra SD, Lichtenthaler SF. Functions of 'A disintegrin and metalloproteases (ADAMs)' in the mammalian nervous system. Cell Mol Life Sci. 2019;76:3055–81. https://doi.org/10.1007/s00018-019-03173-7.
32. Gilchrist SE, Goudarzi S, Hafizi S. Gas6 Inhibits Toll-Like Receptor-Mediated Inflammatory Pathways in Mouse Microglia via Axl and Mer. Front Cell Neurosci. 2020;14:576650. https://doi.org/10.3389/fncel.2020.576650.
33. Ye X-H, Xu Z-M, Shen D, Jin Y-J, Li J-W, Xu X-H, Tong L-S, Gao F. Gas6/Axl signaling promotes hematoma resolution and motivates protective microglial responses after intracerebral hemorrhage in mice. Exp Neurol. 2024;382:114964. https://doi.org/10.1016/j.expneurol.2024.114964.
34. Casden N, Belzer V, Khayari AE, Fatimy RE, Behar O. (2024). Astrocyte-to-microglia communication via Sema4B-Plexin-B2 modulates injury-induced reactivity of microglia. Proc. Natl. Acad. Sci. *121*, e2400648121. https://doi.org/10.1073/pnas.2400648121
35. Elmore MRP, Najafi AR, Koike MA, Dagher NN, Spangenberg EE, Rice RA, Kitazawa M, Matusow B, Nguyen H, West BL, et al. Colony-Stimulating Factor 1 Receptor Signaling Is Necessary for Microglia Viability, Unmasking a Microglia Progenitor Cell in the Adult Brain. Neuron. 2014;82:380–97. https://doi.org/10.1016/j.neuron.2014.02.040.
36. Duclot F, Kabbaj M. The Role of Early Growth Response 1 (EGR1) in Brain Plasticity and Neuropsychiatric Disorders. Front Behav Neurosci. 2017;11:35.

https://doi.org/10.3389/fnbeh.2017.00035.

37. Narendra DP, Youle RJ. The role of PINK1–Parkin in mitochondrial quality control. Nat Cell Biol. 2024;26:1639–51. https://doi.org/10.1038/s41556-024-01513-9.
38. Battis K, Xiang W, Winkler J. The Bidirectional Interplay of α-Synuclein with Lipids in the Central Nervous System and Its Implications for the Pathogenesis of Parkinson's Disease. Int J Mol Sci. 2023;24:13270. https://doi.org/10.3390/ijms241713270.
39. Flores-Leon M, Outeiro TF. More than meets the eye in Parkinson's disease and other synucleinopathies: from proteinopathy to lipidopathy. Acta Neuropathol. 2023;146:369–85. https://doi.org/10.1007/s00401-023-02601-0.
40. Fanning S, Selkoe D, Dettmer U. (2020). Parkinson's disease: proteinopathy or lipidopathy? npj Park.'s Dis. *6*, 3. https://doi.org/10.1038/s41531-019-0103-7
41. Fanning S, Haque A, Imberdis T, Baru V, Barrasa MI, Nuber S, Termine D, Ramalingam N, Ho GPH, Noble T, et al. Lipidomic Analysis of α-Synuclein Neurotoxicity Identifies Stearoyl CoA Desaturase as a Target for Parkinson Treatment. Mol Cell. 2019;73:1001–e10148. https://doi.org/10.1016/j.molcel.2018.11.028.
42. Masuda T, Sankowski R, Staszewski O, Prinz M. Microglia Heterogeneity in the Single-Cell Era. Cell Rep. 2020;30:1271–81. https://doi.org/10.1016/j.celrep.2020.01.010.
43. Grabert K, Michoel T, Karavolos MH, Clohisey S, Baillie JK, Stevens MP, Freeman TC, Summers KM, McColl BW. Microglial brain region–dependent diversity and selective regional sensitivities to aging. Nat Neurosci. 2016;19:504–16. https://doi.org/10.1038/nn.4222.
44. Chitu V, Gokhan Ş, Nandi S, Mehler MF, Stanley ER. Emerging Roles for CSF-1 Receptor and its Ligands in the Nervous System. Trends Neurosci. 2016;39:378–93. https://doi.org/10.1016/j.tins.2016.03.005.
45. Zhang Z, Niu K, Huang T, Guo J, Xarbat G, Gong X, Gao Y, Liu F, Cheng S, Su W, et al. Microglia depletion reduces neurodegeneration and remodels extracellular matrix in a mouse Parkinson's disease model triggered by α-synuclein overexpression. npj Park 's Dis. 2025;11:15. https://doi.org/10.1038/s41531-024-00846-4.
46. Paolicelli RC, Sierra A, Stevens B, Tremblay M-E, Aguzzi A, Ajami B, Amit I, Audinat E, Bechmann I, Bennett M, et al. Microglia states and nomenclature: A field at its crossroads. Neuron. 2022;110:3458–83. https://doi.org/10.1016/j.neuron.2022.10.020.
47. Cerri S, Mus L, Blandini F. Parkinson's Disease in Women and Men: What's the Difference? J Park 's Dis. 2019;9:501–15. https://doi.org/10.3233/jpd-191683.
48. Ekstrand MI, Terzioglu M, Galter D, Zhu S, Hofstetter C, Lindqvist E, Thams S, Bergstrand A, Hansson FS, Trifunovic A, et al. Progressive parkinsonism in mice with respiratory-chain-deficient dopamine neurons. Proc Natl Acad Sci USA. 2007;104:1325–30. https://doi.org/10.1073/pnas.0605208103.
49. Hupe M, Li MX, Gillner KG, Adams RH, Stenman JM. Evaluation of TRAP-sequencing technology with a versatile conditional mouse model. Nucleic Acids Res. 2014;42:e14. https://doi.org/10.1093/nar/gkt995.

50. Tiklova K, Björklund AK, Lahti L, Fiorenzano A, al, et B, Gillberg L, Volakakis N, Yokota C, Hilscher MM, Hauling T, et al. Single-cell RNA sequencing reveals midbrain dopamine neuron diversity emerging during mouse brain development. Nat Commun. 2019;10:581. https://doi.org/10.1038/s41467-019-08453-1.
51. Preibisch S, Saalfeld S, Tomancak P. Globally optimal stitching of tiled 3D microscopic image acquisitions. Bioinformatics. 2009;25:1463–5. https://doi.org/10.1093/bioinformatics/btp184.
52. Zeisel A, Muñoz-Manchado AB, Codeluppi S, Lönnerberg P, Manno GL, Juréus A, Marques S, Munguba H, He L, Betsholtz C, et al. Brain structure. Cell types in the mouse cortex and hippocampus revealed by single-cell RNA-seq. Sci (New York NY). 2015;347:1138–42. https://doi.org/10.1126/science.aaa1934.
53. Hao Y, Hao S, Andersen-Nissen E, Mauck WM, Zheng S, Butler A, Lee MJ, Wilk AJ, Darby C, Zager M, et al. Integrated analysis of multimodal single-cell data. Cell. 2021;184:3573–e358729. https://doi.org/10.1016/j.cell.2021.04.048.
54. Hafemeister C, Satija R. Normalization and variance stabilization of single-cell RNA-seq data using regularized negative binomial regression. Genome Biol. 2019;20:296. https://doi.org/10.1186/s13059-019-1874-1.
55. McGinnis CS, Murrow LM, Gartner ZJ. DoubletFinder: Doublet detection in single-cell RNA sequencing data using artificial nearest neighbors. bioRxiv. 2018;352484. https://doi.org/10.1101/352484.
56. He L, Davila-Velderrain J, Sumida TS, Hafler DA, Kellis M, Kulminski AM. Commun Biol. 2021;4:629. https://doi.org/10.1038/s42003-021-02146-6. NEBULA is a fast negative binomial mixed model for differential or co-expression analysis of large-scale multi-subject single-cell data.
57. Korotkevich G, Sukhov V, Budin N, Shpak B, Artyomov MN, Sergushichev A. Fast gene set enrichment analysis. bioRxiv. 2021;060012. https://doi.org/10.1101/060012.
58. Fleming SM, Ekhator OR, Ghisays V. Assessment of Sensorimotor Function in Mouse Models of Parkinson's Disease. J Vis Exp : JoVE. 2013;50303. https://doi.org/10.3791/50303.

Figures

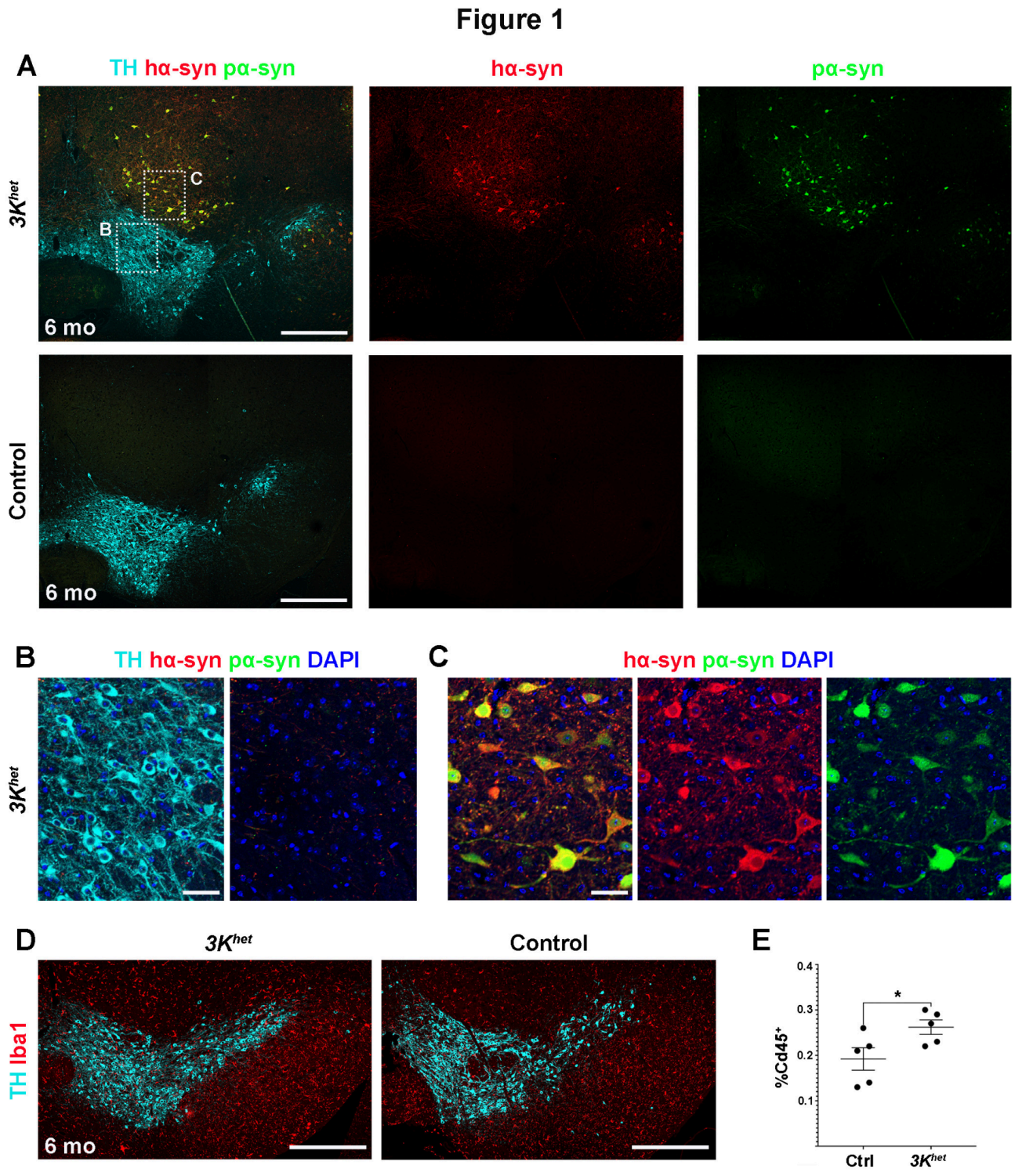


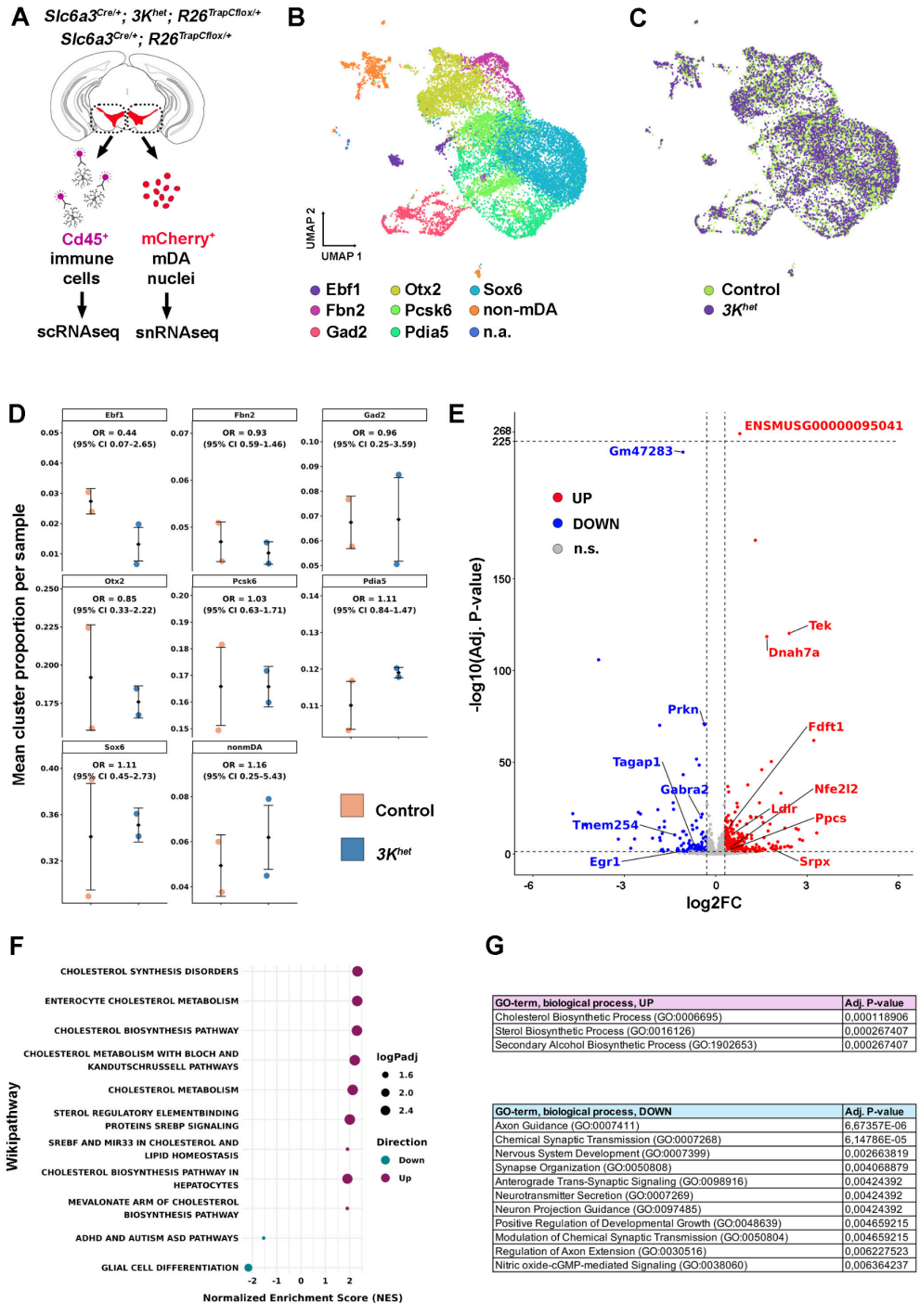
Figure 1

Expression of human alfa-synuclein in *3K*^{het} ventral midbrain

A) Immunohistochemistry (IHC) for human alfa-synuclein (ha-syn) and phospho alfa-synuclein S129 (pa-syn) in 6 months old ventral midbrain of *3K*^{het} and control mice. B-C) Close-ups of the boxed areas shown in A). D) Immunohistochemistry for TH and general microglial marker Iba1 in the ventral midbrain of 6

months old *3K*^{het} and control animals. E) Quantification result of Cd45^{+} immune cells by FACS from the ventral midbrain tissue of 6 months old *3K*^{het} (n=5) and control (n=5). * p<0.05. Unpaired t-test. Tiled images in A, D. Scalebars 500 um in A, D, 50 um in B, C.

Figure 2



GO-term, biological process, UP	Adj. P-value
Cholesterol Biosynthetic Process (GO:0006695)	0,000118906
Sterol Biosynthetic Process (GO:0016126)	0,000267407
Secondary Alcohol Biosynthetic Process (GO:1902653)	0,000267407

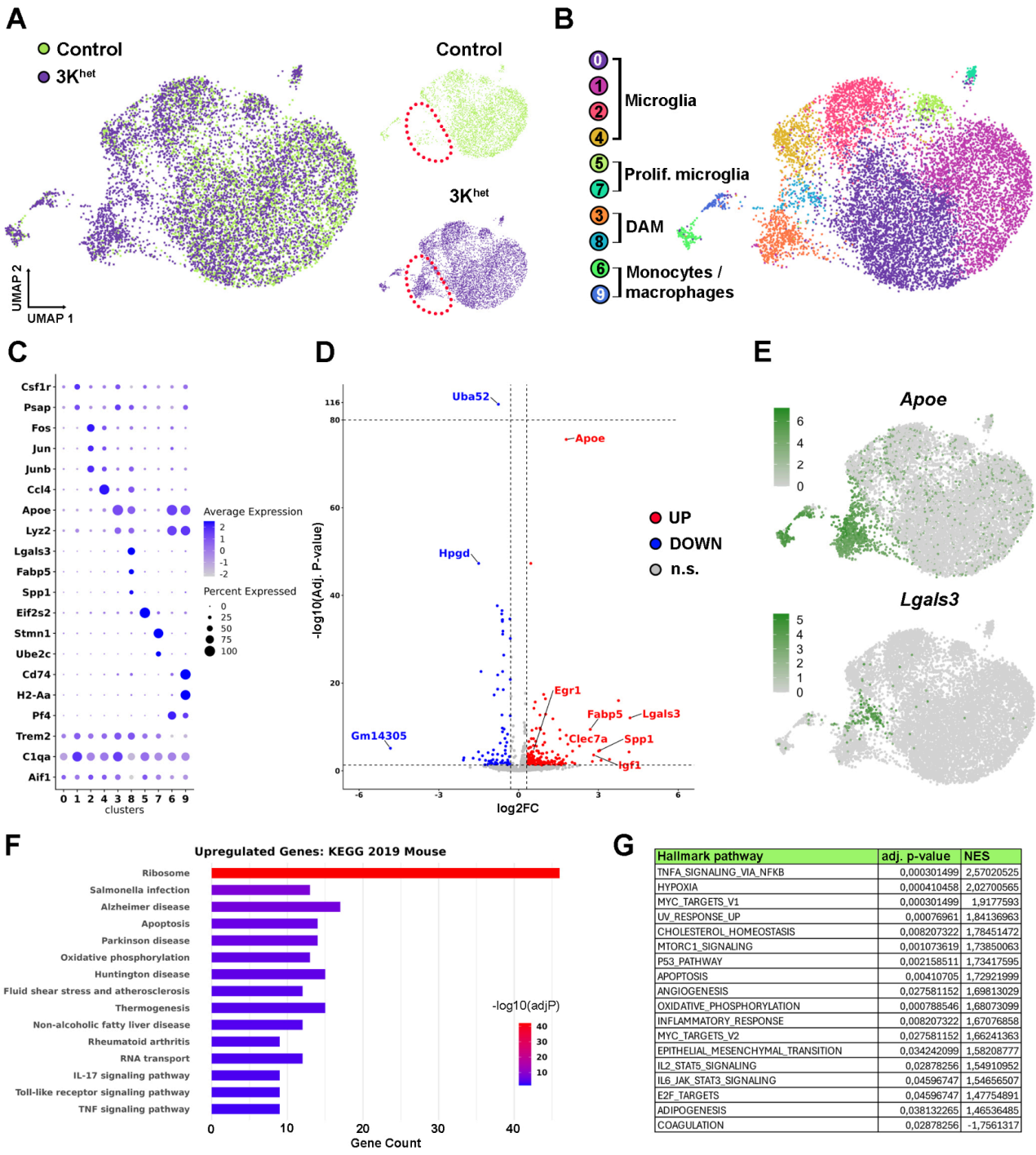
GO-term, biological process, DOWN	Adj. P-value
Axon Guidance (GO:0007411)	6,67357E-06
Chemical Synaptic Transmission (GO:0007268)	6,14786E-05
Nervous System Development (GO:0007399)	0,002663819
Synapse Organization (GO:0050808)	0,004068879
Anterograde Trans-Synaptic Signaling (GO:0098916)	0,00424392
Neurotransmitter Secretion (GO:0007269)	0,00424392
Neuron Projection Guidance (GO:0097485)	0,00424392
Positive Regulation of Developmental Growth (GO:0048639)	0,004659215
Modulation of Chemical Synaptic Transmission (GO:0050804)	0,004659215
Regulation of Axon Extension (GO:0030516)	0,006227523
Nitric oxide-cGMP-mediated Signaling (GO:0038060)	0,006364237

Figure 2

Single nuclear RNA sequencing of midbrain dopamine neurons from *3K*^{het} and control mice

A) A schematic showing the approximate region of the midbrain from where immune cells and mDA nuclei were collected for sorting and sequencing. B) UMAP plot of all cells in the mDA dataset, both from *3K*^{het} and control, colour coded for different mDA subclusters. C) UMAP plot showing the distribution of control and *3K*^{het} cells in the dataset. D) Mean territory proportions per sample across the clusters (territories) between *3K*^{het} and control, calculated using a quasibinomial GLM. For all comparisons, 95% CI encompass the null value OR=1 (n=2 samples per genotype). E) A volcano plot showing selected significantly different (adj.p-value <0.05, abs(log2FC)>0.3) genes between *3K*^{het} and control neurons. UP=higher expression in *3K*^{het}, DOWN=lower expression in *3K*^{het}. F) GSEA Wikipathways with significant differential enrichment in *3K*^{het} neurons compared to control. logPadj = -log10(adjusted p-value). G) GO-terms for biological processes that were significantly up- or downregulated in *3K*^{he} compared to the control.

Figure 3



G

Hallmark pathway	adj. p-value	NES
TNFA_SIGNALING_VIA_NFKB	0,000301499	2,57020525
HYPOXIA	0,000410458	2,02700565
MYC_TARGETS_V1	0,000301499	1,9177593
UV_RESPONSE_UP	0,00076961	1,84136963
CHOLESTEROL_HOMEOSTASIS	0,008207322	1,78451472
MTORC1_SIGNALING	0,001073619	1,73850063
P53_PATHWAY	0,002158511	1,73417595
APOPTOSIS	0,00410705	1,72921999
ANGIOGENESIS	0,027581152	1,69813029
OXIDATIVE_PHOSPHORYLATION	0,000788546	1,68073099
INFLAMMATORY_RESPONSE	0,008207322	1,67076858
MYC_TARGETS_V2	0,027581152	1,66241363
EPITHELIAL_MESENCHYMAL_TRANSITION	0,034242099	1,58208777
IL2_STAT5_SIGNALING	0,02878256	1,54910952
IL6_JAK_STAT3_SIGNALING	0,04596747	1,54656507
E2F_TARGETS	0,04596747	1,47754891
ADIPOGENESIS	0,038132265	1,46536485
COAGULATION	0,02878256	-1,7561317

Figure 3

Single cell RNA sequencing of immune cells in *3K*^{het} and control midbrain

A) UMAP plot showing the distribution of control and *3K*^{het} cells in the dataset. Encircled areas of the UMAPs highlight the area containing mostly *3K*^{het} cells. B) UMAP plot showing ten clusters of the dataset corresponding to monocytes, macrophages, and different types of microglia. C) A dot plot of

selected genes enriched in the different clusters, together with general microglial marker genes. D) A volcano plot depicting selected genes either up- or downregulated (adj.p-value <0.05, abs(log2FC)>0.3) in *3K*^{het} immune cells compared to control. E) The expression of *Apoe* and *Lgals3* plotted on the UMAP. F) Significantly upregulated KEGG pathway terms in *3K*^{het} t immune cells. G) The significantly upregulated GSEA Hallmark pathways in *3K*^{het} immune cells.

Figure 4

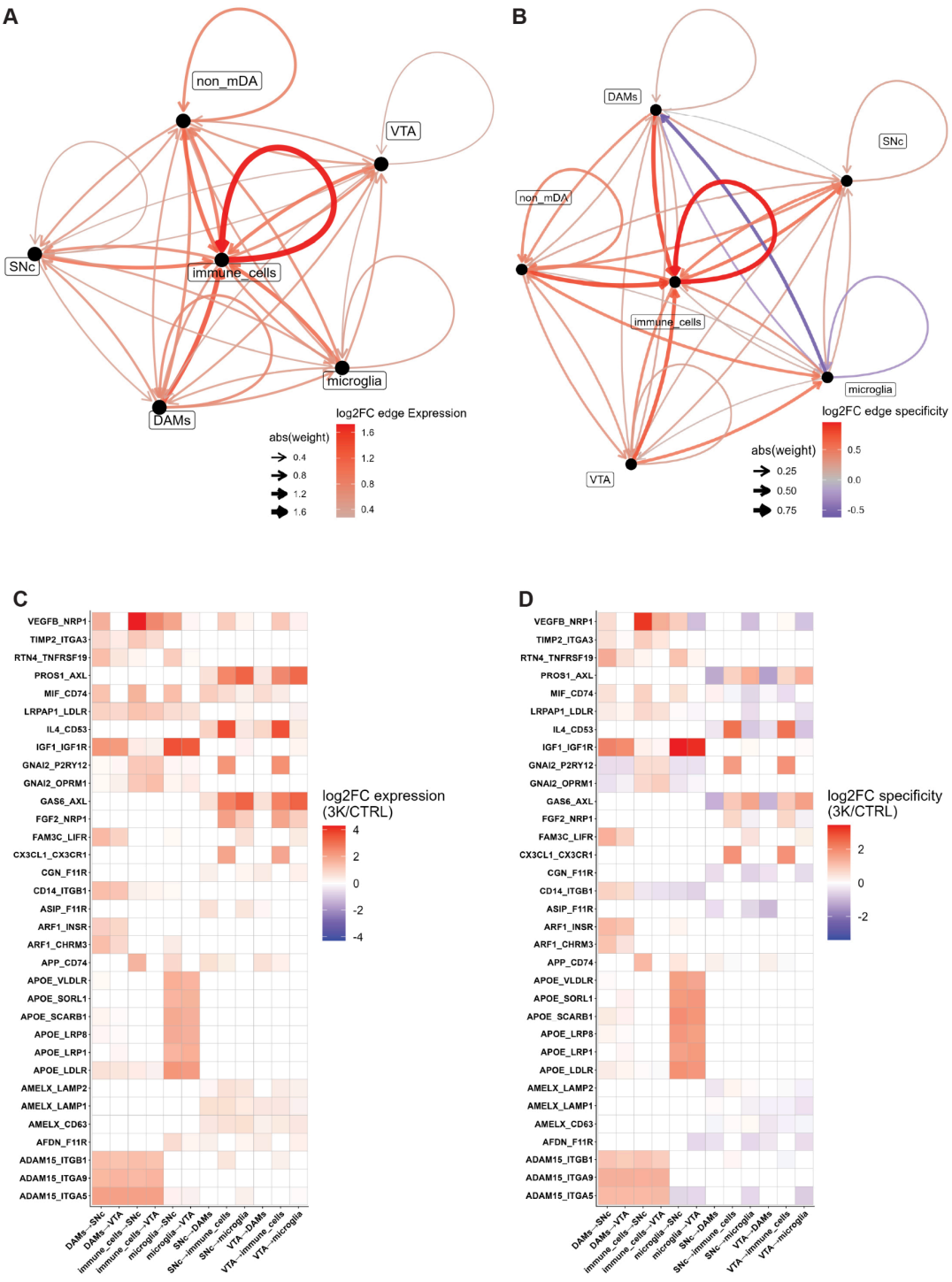


Figure 4

Cell interactome for ligand-receptor pairs with higher expression weights in *3K*^{het}

A-B) Changes in cell interaction networks between *3K*^{het} and control among cell-types measured in ligand-receptor (LR) expression weights (A) and LR specificity weights (B), calculated as log2FC, based on a set of edges (LR pairs) with higher expression weights in the target dataset (3K). C-D) Heatmaps of log2FC (*3K*^{het}/Ctrl) of expression (C) and specificity (D) edge weights for the top 5 LR pairs in Log2FC edge expression weight per cell-type pair. Selection was done based on Log2FC edge expression weight and the same LR pairs were plotted for specificity. LR = Ligand-Receptor, red = higher in *3K*^{het}, blue = higher in control. Arrows: biological direction from sender (ligand-expressing) → receiver (receptor-expressing), arrow thickness indicates the interaction magnitude.

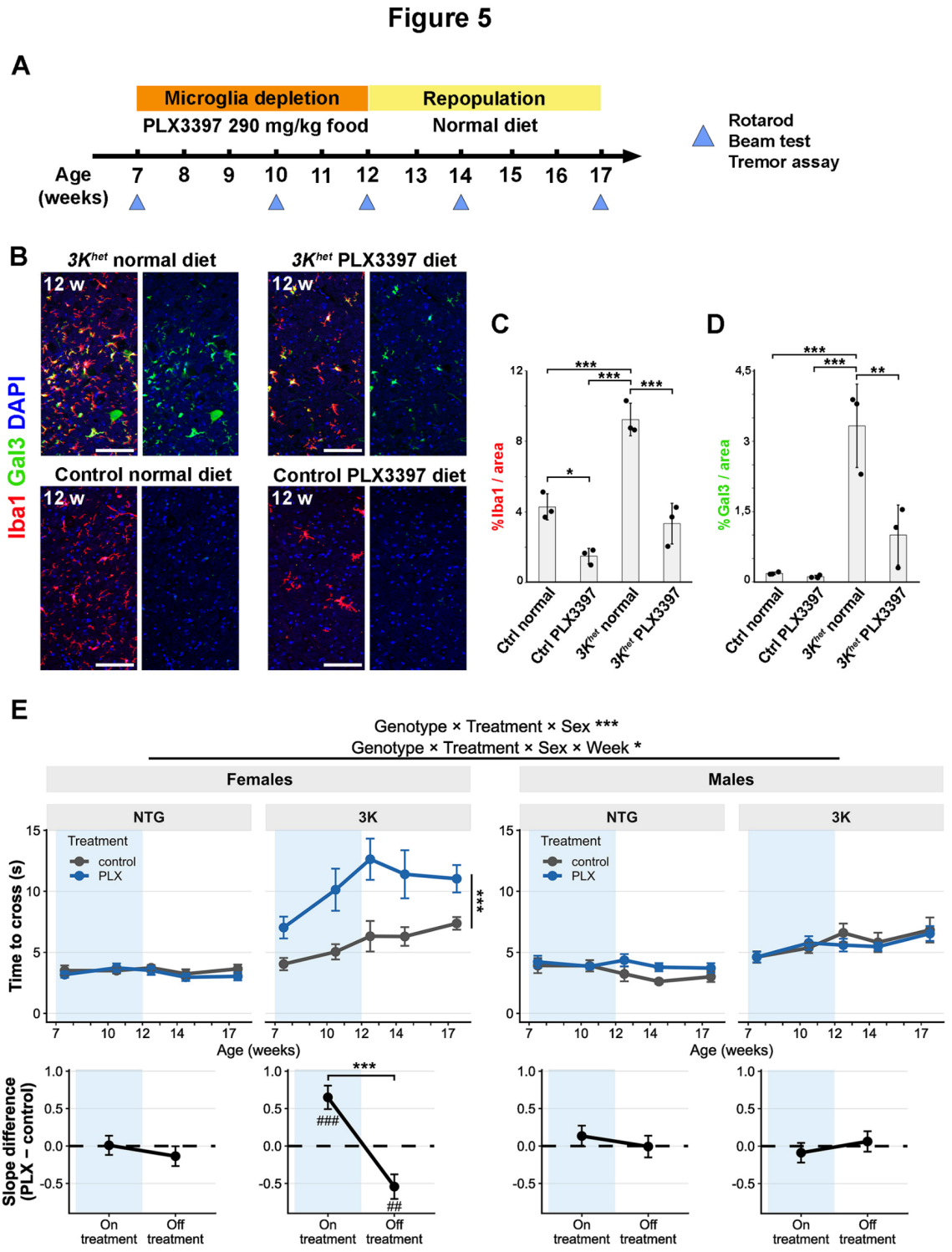


Figure 5

Depletion of microglia with PLX3397-supplemented diet

A) Schematic of the depletion plan, with timepoints of behavioral testing indicated with blue triangles. B) Representative IHC stainings for Iba1 and Gal3 of *3K*^{het} and control midbrains, fed either normal or PLX3397-supplemented diet, after the 5-week depletion phase. The left panel shows the overlay of Iba1,

Gal3, and DAPI, and the right panel shows Gal3 and DAPI only. Scalebars 100 um. C-D) Quantification of $Iba1^+$ and $Gal3^+$ signal per area. N=3 for each group. *** p<0.001, ** p<0.01, *p<0.05. One-way ANOVA with Tukey. E) Beam test result divided by sex and genotype. Upper part depicts the time to cross and lower part depicts the slope difference between treatment and control groups. Blue background indicates depletion phase, and white background indicates repopulation phase. n=4-6 per group *** p<0.001, *p<0.05 4-way repeated measures ANOVA. NTG, non-transgenic (control) animal.

Supplementary Files

This is a list of supplementary files associated with this preprint. Click to download.

- supplfigsmergedcompressed.pdf
- suppltable7.xlsx
- suppltable2.xlsx
- suppltable13.xlsx
- suppltable14.xlsx
- suppltable9.xlsx
- suppltable1.xlsx
- suppltable5.xlsx
- suppltable6.xlsx
- suppltable8.xlsx
- suppltable4.xlsx
- suppltable12.xlsx
- suppltable10.xlsx
- suppltable3.xlsx
- suppltable11.xlsx
- SupplementaryFigureLegends.docx